

Thermally unstable convection with applications to chemical vapor deposition channel reactorst

GREG EVANS

Computational Mechanics Division, Sandia National Laboratories, Livermore, CA 94550, U.S.A.

and

RALPH GREIF

Mechanical Engineering Department, University of California, Berkeley, CA 94720, U.S.A.

(Received 31 January 1992 and in final form 1 December 1992)

Abstract—The three dimensional, thermally unstable flow and heat transfer of a gas have been studied in a horizontal channel with applications to chemical vapor deposition (CVD). The cases examined include flows that exhibit a longitudinal roll instability and a combination of both transverse, traveling waves and longitudinal rolls. Detailed results are presented for two values of the temperature ratio $\varepsilon = (T_1 - T_0)/T_0 = 0.01$ and 2.33 (helium), Grashof number $Gr = g\beta H^3/\nu_0^2 = 125\,000$, Prandtl number $Pr = \nu_0/\alpha_0 = 2/3$, aspect ratios $L/H = 10$ and $W/H = 2$. For $\varepsilon = 0.01$ and Reynolds number $Re = \bar{u}H/\nu_0 = 250$, longitudinal rolls result whereas for $Re = 100$ a combination of transverse waves and longitudinal rolls occurs. For $\varepsilon = 2.33$ and $Re = 100$ the longitudinal roll instability is present.

INTRODUCTION

CHEMICAL vapor deposition (CVD) involves the transport of reacting gases in a reactor with deposition occurring on heated surfaces (Jensen [1], Coltrin *et al.* [2], Giling [3], Moffat and Jensen [4], Fotiadis *et al.* [5], Kleijn *et al.* [6], Chiu and Rosenberger [7]). The goals of increased rates of deposition (occurring generally at higher pressure) and increased uniformity of films can be difficult to achieve due to unstable and recirculating fluid flow which in many cases is due to the effects of buoyancy. An understanding of these phenomena in CVD reactors is necessary to optimize reactor operating parameters.

Typically, horizontal channel flow CVD reactors are operated in regimes where thermal instabilities may be present. For example, Ouazzani and Rosenberger [8] have studied horizontal MOCVD reactors numerically and compared their results with the experimental data of Van de Ven *et al.* [9]. In a steady analysis they obtained thermal instabilities consisting of longitudinal rolls even for subcritical Rayleigh numbers. Recently, Nyce *et al.* [10] carried out an experimental and numerical study of mixed convection in a horizontal channel at Rayleigh numbers typical of CVD operating conditions. Their results show variations in both the axial and transverse direc-

tions which are consistent with the presence of both longitudinal roll and transverse wave instabilities. In a comprehensive review of flow phenomena in CVD, Jensen *et al.* [11] discuss flow instabilities in horizontal reactors. They point out the effects of these instabilities on the magnitude and uniformity of the deposition. Thermal instability in the form of longitudinal rolls has also been predicted by Kleijn [12] for flow in horizontal CVD reactors.

Instabilities that alter Poiseuille base flows in horizontal channels heated from below are characterized by longitudinal rolls provided the Rayleigh number is above the critical value of 1708, regardless of the Reynolds number (Gage and Reid [13]). As the Rayleigh number is increased the flow becomes unstable to disturbances in the form of transverse waves (Clever and Busse [14]); this is a function of the Reynolds number and becomes more pronounced as the Reynolds number is decreased. The flow also depends on the thermal boundary conditions on the lateral surfaces of the channel; for small Re , Platten and Legros [15] have shown that the critical Ra is smaller for traveling transverse waves than for longitudinal rolls when the presence of lateral boundaries is considered. The present study has been carried out to provide new results for unsteady, three dimensional flows that include combinations of traveling transverse wave and longitudinal roll instabilities.

Our previous three dimensional study [16] considered buoyancy dominated flows at small Reynolds and moderate Grashof numbers. In that work the

† This work was supported by the United States Department of Energy.

NOMENCLATURE

g	acceleration of gravity	W	channel width
Gr	Grashof number, $g\epsilon H^3/\nu_0^2$	x	dimensionless axial coordinate, x^*/H
H	channel height	Δx	dimensionless grid spacing in axial direction, $\Delta x^*/H$
k	thermal conductivity	y	dimensionless vertical coordinate, y^*/H
L	channel length	Δy	dimensionless grid spacing in vertical direction, $\Delta y^*/H$
$Nu_{l,u}$	local Nusselt numbers on lower and upper surfaces, $[q_{l,u}^* H/k_o(T_1 - T_o)] = -(k/k_o)(\partial\Theta/\partial y) _{y=0,1}$	z	dimensionless spanwise coordinate, z^*/H
$\bar{N}u_{l,u}$	average Nusselt numbers on lower and upper surfaces, $[(\bar{q}_{l,u}^* H/k_o(T_1 - T_o))] = (H^2/W \cdot L) \times \sum_{l,u} Nu_{l,u} \Delta x \Delta z$	Δz	dimensionless grid spacing in spanwise direction, $\Delta z^*/H$.
Pr	Prandtl number, $\nu_0/\alpha_0 = 2/3$ for helium	Greek symbols	
$Q_{l,u}^*$	total dimensional heat flow rate from lower and upper surfaces, $\sum_{l,u} q_{l,u}^* \Delta x^* \Delta z^*$	α	thermal diffusivity
$q_{l,u}^*$	dimensional local heat flux at lower and upper surfaces, $-k(\partial T/\partial y^*) _{y=0,H}$	ϵ	temperature ratio, $(T_1 - T_o)/T_o$
$q_{l,u}^*$	dimensional average heat flux at lower and upper surfaces, $Q_{l,u}^*/(W \cdot L)$	ρ	density
Ra	Rayleigh number, $g\epsilon H^3/(\nu_o \alpha_o) = Gr \cdot Pr$	ν	kinematic viscosity
Re	Reynolds number, $\bar{u}H/\nu_o$	Θ	dimensionless temperature, $(T - T_o)/(T_1 - T_o)$.
t	dimensionless time	Subscripts and superscripts	
T	temperature	l	conditions at hot lower surface of channel ($y = 0$)
T_l	lower surface temperature	o	dimensional quantities evaluated at temperature $T_o = 300$ K
T_u	upper surface temperature = $T_o = 300$ K	u	conditions at cold upper surface of channel ($y = 1$), $T_u = T_o$
\bar{u}	average dimensional axial velocity at inlet of channel	*	dimensional quantity.

instability consisted primarily of periodic traveling transverse waves (essentially translating Benard cells); the longitudinal roll component was small. The present study, at larger values of the Reynolds and Grashof numbers, is more typical of the operation of horizontal CVD reactors; the results show significantly more complex flow fields due to the stronger interactions between buoyancy and forced flow. The resulting unstable phenomena yield two structures; one dominated by forced convection consisting of longitudinal rolls whose axes are aligned with the bulk flow and the other consisting of the interaction between the longitudinal rolls and transverse traveling waves. It is shown below that for small temperature differences ($\epsilon = 0.01$) and $Re = 250$ the flow consists primarily of longitudinal rolls (for $Gr = 1.25 \times 10^5$) and is less complex than that occurring for $Re = 100$ ($Gr = 1.25 \times 10^5$) where the relative effect of buoyancy is greater. Longitudinal rolls are also the dominant flow pattern for large temperature differences ($\epsilon = 2.33$) and $Re = 100$.

MODEL AND SOLUTION METHOD

The unsteady, three dimensional, variable property Navier-Stokes and energy equations are presented in

ref. [16] for a horizontal channel flow reactor and are not repeated here. Dimensionless equations are solved using the channel height H , buoyant velocity $\sqrt{(g\epsilon H)}$, time $\sqrt{(H/(g\epsilon))}$, pressure $\rho_o g\epsilon H$, and temperature difference $(T_1 - T_o)$ as the characteristic quantities. The fluid properties are made dimensionless with the quantities evaluated at the temperature T_o . We emphasize that the Boussinesq approximation is not invoked. The higher Reynolds and Grashof numbers studied here result in phenomena that differ markedly from the previous work. It is also noted that the boundary conditions differ from those of ref. [16] in that the inlet gas temperature is now equal to the cold upper surface temperature, resulting in a thermally developing flow along the lower heated surface of the channel. This is a more realistic thermal boundary condition for the operation of many horizontal CVD reactors. The axial aspect ratio is now larger, 10 instead of 8. The flow has a fully developed inlet velocity profile, adiabatic side walls, and a hot isothermal lower surface (Fig. 1). Outflow boundary conditions at $x = L/H$ are obtained by setting the x (axial) derivatives of the velocity components and temperature to zero. To solve the governing equations, the control volume formulation is used in conjunction with a finite difference discretization (central differ-

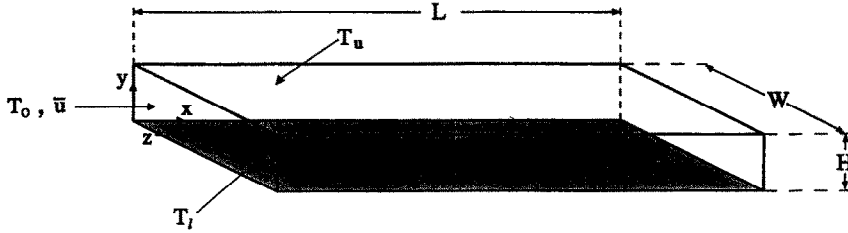


FIG. 1. Horizontal channel reactor geometry and coordinate system.

ences are used for all spatial derivatives, and backward differences are applied to the time derivatives). The method of solution utilizes a staggered grid with velocities located on control volume faces and temperature and pressure located at control volume centers. The numerical algorithm is based on the TEACH formulation (Gosman and Pun [17]); the SIMPLER method is used to determine the pressure field (Patankar [18]).

RESULTS AND DISCUSSION

The flow and energy transfer are characterized by a broad range of phenomena encompassing extremely complex flow patterns and heat transfer variations. These phenomena are discussed below.

Small temperature differences ($\epsilon = 0.01$)

Steady longitudinal rolls ($Re = 250, Gr = 1.25 \times 10^5$).
The case $\epsilon = 0.01, Re = 250, Gr = 1.25 \times 10^5$,

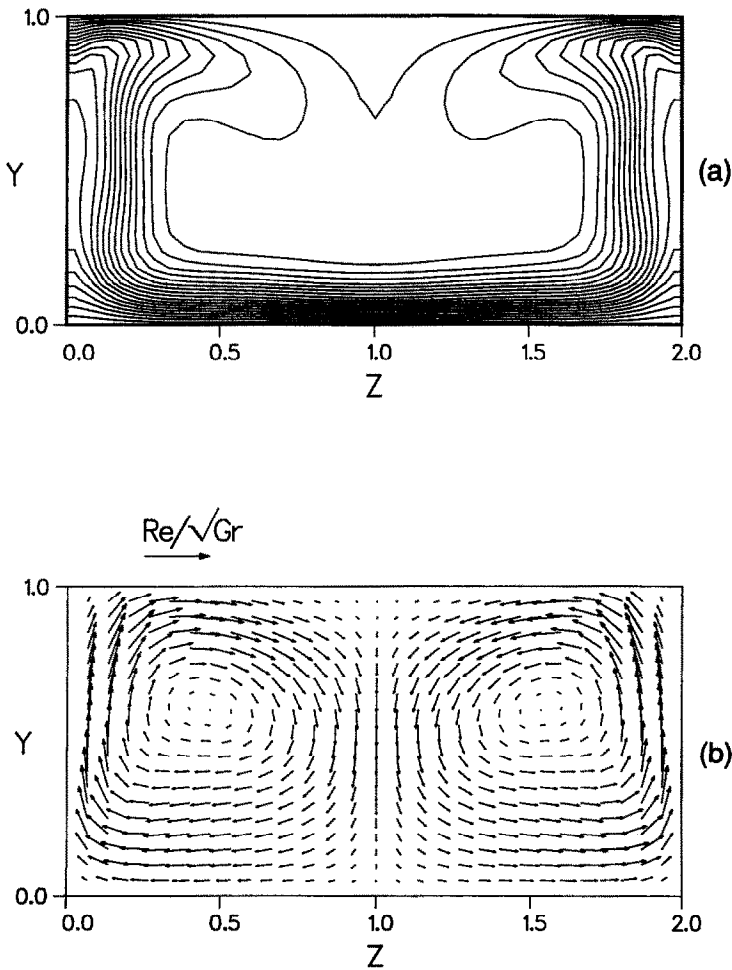


FIG. 2. Temperature and velocity fields in a transverse cross-sectional (yz) plane ($x = 6.01$) for $Re = 250, Gr = 1.25 \times 10^5, \epsilon = 0.01$; (a) temperature contours (min 0.05, max 0.95, inc 0.05); (b) velocity arrows (reference arrow length corresponds to average dimensionless velocity at channel inlet: Re/\sqrt{Gr}).

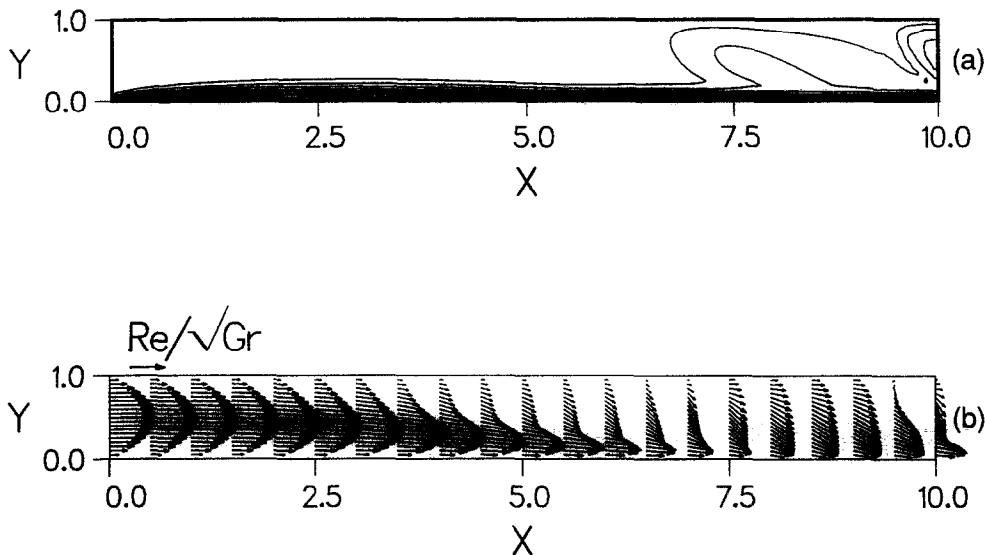


FIG. 3. Temperature and velocity fields in the vertical central (xy) plane ($z = 1.0$) of the channel for $Re = 250$, $Gr = 1.25 \times 10^5$, $\epsilon = 0.01$; (a) temperature contours (min 0.1, max 0.9, inc 0.1); (b) velocity arrows (reference arrow length corresponds to average dimensionless velocity at channel inlet: Re/\sqrt{Gr}).

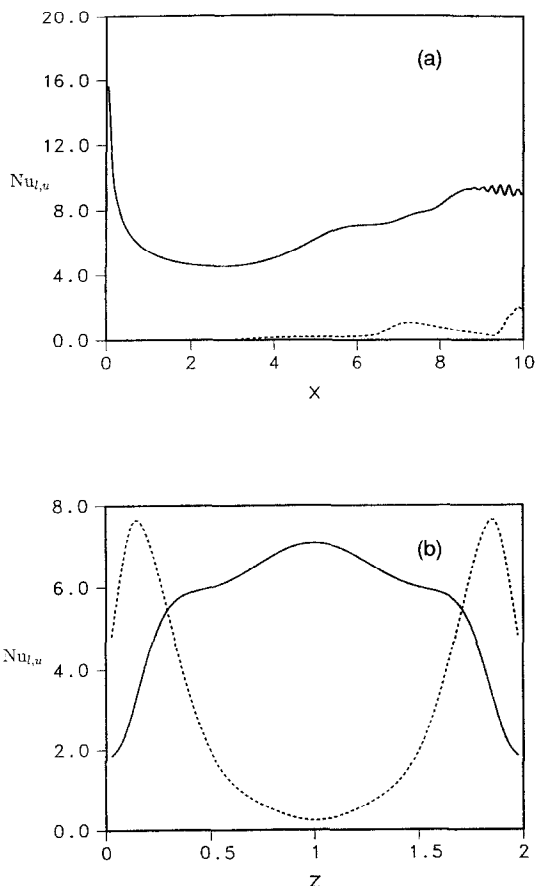


FIG. 4. Local Nusselt numbers on the lower hot surface (—) and the upper cold surface (---) of the channel for $Re = 250$, $Gr = 1.25 \times 10^5$, $\epsilon = 0.01$; (a) for the vertical central plane ($z = 1.0$); (b) for a transverse cross-sectional (yz) plane ($x = 6.01$).

$10 \times 1 \times 2$ (x, y, z) channel dimensions results in steady conditions. Over a transverse cross-section (yz plane), longitudinal roll structures are present (Figs. 2(a) and (b) at $x = 6.01$). The symmetry about $z = 1.0$ is a result of the symmetry of the problem and the imposed boundary conditions on the vertical side walls; it is not the result of imposing symmetry conditions at $z = 1.0$ (i.e. the calculations are carried out from $z = 0$ to 2 and no condition is imposed at $z = 1.0$). Over an axial plane (xy plane) the high flow rate combined with an inlet gas temperature that is equal to that of the cold upper surface results in a thermally developing field near the lower surface; the instability develops in the downstream half of the channel (Figs. 3(a) and (b) at $z = 1.0$).

The axial variation of the lower surface Nusselt number Nu_l at $z = 1.0$ (Fig. 4(a)) shows a thermal boundary layer variation corresponding to the temperature difference at the inlet between the gas and the lower heated surface as indicated above. There is a minimum at $x \approx 3$ which is followed by a gradual increase in the heat transfer associated with the onset of the thermal instability; this is accompanied by a nonzero value of the upper surface Nusselt number Nu_u . The variation of the Nusselt number in a transverse cross-section at the axial position $x = 6.01$ is dramatically different on the upper and lower surfaces (Fig. 4(b)). This variation corresponds to the longitudinal roll instability with hot fluid from the lower surface rising along the adiabatic side walls of the channel and impinging on the cold upper surface; this results in the large value of Nu_u near the side walls. The downward moving fluid near $z = 1.0$ (Fig. 2(b)) gives rise to the large value of Nu_l (Fig. 4(b)) in the central region. Surface maps of Nu_l and Nu_u (Figs.

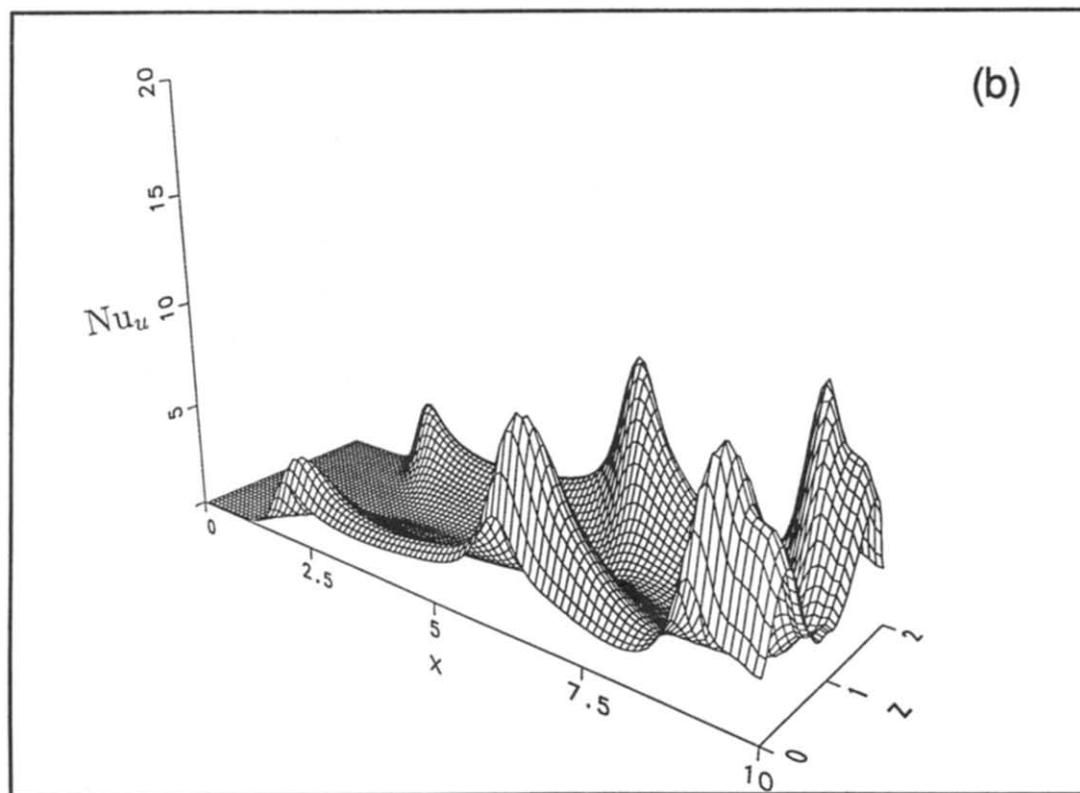
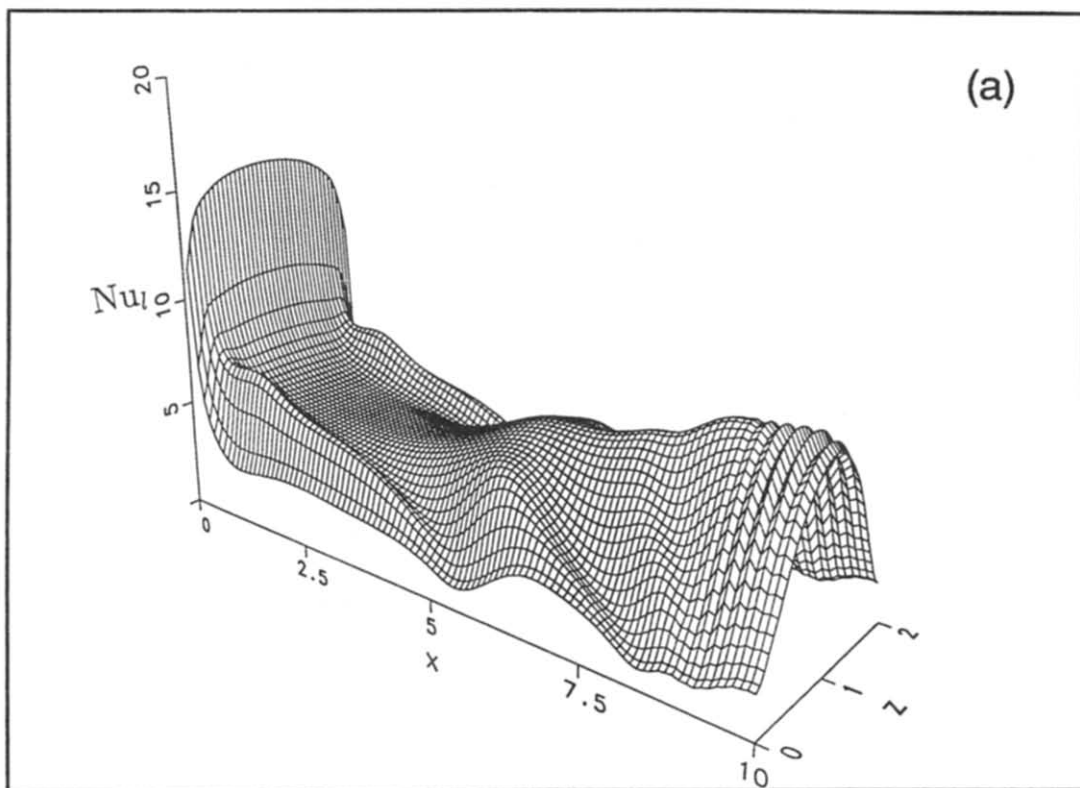


FIG. 5. Surface maps of the local Nusselt numbers for $Re = 250$, $Gr = 1.25 \times 10^5$, $\epsilon = 0.01$; (a) on the lower hot surface; (b) on the upper cold surface.

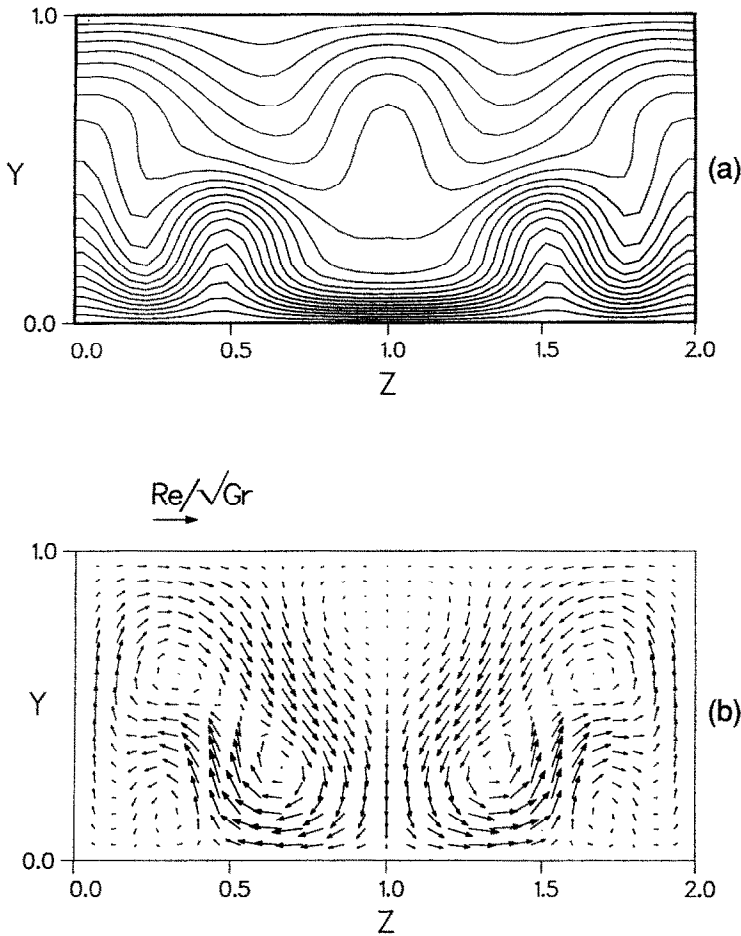


FIG. 6. Temperature and velocity fields in a transverse cross-sectional (yz) plane ($x = 6.18$) for $Re = 100$, $Gr = 1.25 \times 10^5$, $\varepsilon = 0.01$, $t = 80$; (a) temperature contours (min 0.05, max 0.95, inc 0.05); (b) velocity arrows (reference arrow length corresponds to average dimensionless velocity at channel inlet: Re/\sqrt{Gr}).

5(a) and (b) show the effect of the instability on the lower and upper surface heat transfer. The spatially averaged Nusselt numbers on the lower (\overline{Nu}_l) and upper (\overline{Nu}_u) surfaces are approximately 5.1 and 1.7, respectively.

Combination of longitudinal rolls and transverse waves ($Re = 100$, $Gr = 1.25 \times 10^5$). As the Reynolds number is decreased from 250 for $Gr = 1.25 \times 10^5$, the flow becomes unsteady and complex. For $Re = 100$, the ratio of the characteristic buoyant to forced velocities, \sqrt{Gr}/Re , is 3.5, and the nondimensional time for transport through the channel at the average convective speed, \bar{u} , is: $\tau_{ch} = (L/H) \cdot \sqrt{Gr}/Re = 35$. For the results presented here at $Re = 100$, $Gr = 1.25 \times 10^5$, the equations were integrated to $t = 81$, corresponding to 2.3 average transit times through the channel. After $t \approx 50$, the flow became quasi-steady, with time dependencies confined primarily to the downstream 40% of the channel; these irregular time variations resulted in variations in the average Nusselt numbers on the lower and upper surfaces of the channel ($\overline{Nu}_{l,u}$) of 5 and 10%, respectively.

Over a transverse cross-section, longitudinal roll structures are again present (Figs. 6(a) and (b) at $x = 6.18$, $t = 80$). Over an axial plane there is now a more complex flow pattern with recirculating flow regions and also several transverse waves (Figs. 7(a) and (b) at $z = 1.0$, $t = 80$). In comparing Figs. 3(a) and (b) ($Re = 250$) with Figs. 7(a) and (b) ($Re = 100$), note that at the lower Re the instability begins at a smaller streamwise position. Hence the complex flow structure for $Re = 100$ in Figs. 7(a) and (b) is closely related to the fact that the instability begins nearer to the inlet and develops in the remainder of the channel (from $x = 2.7$ to $x = 10$). Indeed, it is anticipated that for large Re and small channel lengths, the instability would not be present. The variations of the temperature and velocity fields in horizontal (xz) planes are shown in Figs. 8(a)–(f). In Figs. 8(a)–(c), regions of hot rising fluid are evident between the centerline of the channel and the side walls. Figures 8(d)–(f) show the severe depletion of streamwise motion near the centerline and the regions of backflow in the upper half ($y > 0.5$) of the channel.

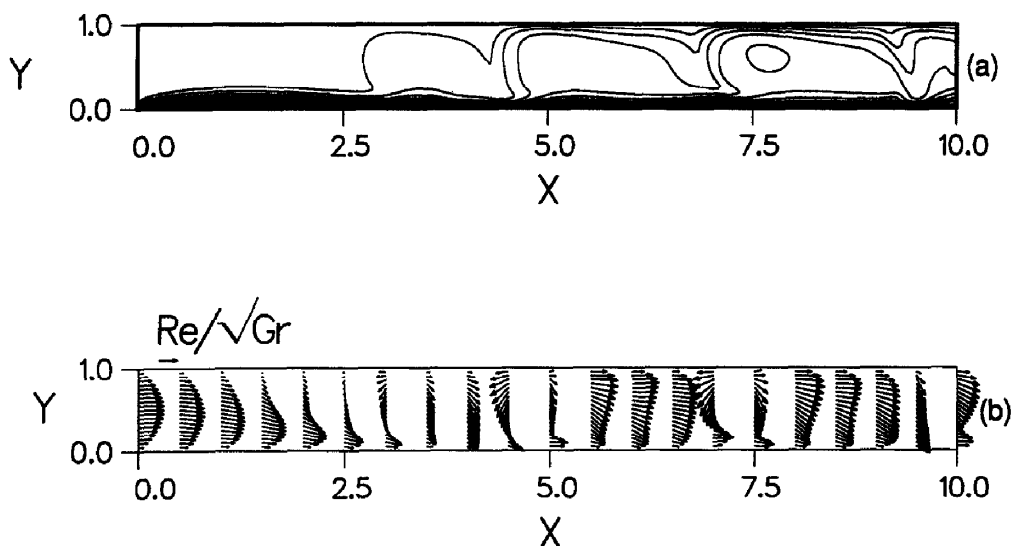


FIG. 7. Temperature and velocity fields in the vertical central (xy) plane ($z = 1.0$) of the channel for $Re = 100$, $Gr = 1.25 \times 10^5$, $\varepsilon = 0.01$, $t = 80$; (a) temperature contours (min 0.1, max 0.9, inc 0.1); (b) velocity arrows (reference arrow length corresponds to average dimensionless velocity at channel inlet: Re/\sqrt{Gr}).

The extreme complexity of the flow and heat transfer is revealed in surface maps of the local heat transfer, $Nu_{i,u}$, on the lower and upper surfaces of the channel in Figs. 9(a)–(d). Large peaks and valleys in Nu_i (Fig. 9(a)) occur in both the streamwise (x) and lateral (z) directions. Large peaks in Nu_u near the side walls occur periodically in the streamwise direction (Figs. 9(b)–(d)) and correspond with undulations in the deep trough in Nu_u along the centerline ($z = 1.0$).

The axial variation of $Nu_{i,u}$ along the centerline for $Re = 100$ shown in Fig. 10(a) is in contrast with the axial variation of the heat transfer for $Re = 250$ (Fig. 4(a)), which essentially exhibits a steady increase in Nu_i after the onset of the instability. For $x < 5$, this leads to enhanced heat transfer for $Re = 100$ in comparison to $Re = 250$, whereas for $x > 5$, Nu_i (along the centerline, $z = 1.0$) for $Re = 100$ is reduced compared with the values for $Re = 250$.

Figure 10(b) shows the variation of the Nusselt numbers, $Nu_{i,u}$ across the channel at $x = 6.18$. Earlier we noted that the differences between Nu_u and Nu_l over a transverse cross-section (Fig. 4(b)) for $Re = 250$ are related primarily to the longitudinal roll structure; now, for $Re = 100$, Nu_l has a distinct triple peak pattern which contrasts with the broad maximum that occurs for $Re = 250$; Nu_u also has a triple peak in contrast to the large peaks at the side walls for $Re = 250$. The triple peaks in $Nu_{i,u}$ are related to the complex flow pattern (partially indicated in the transverse cross-section shown in Fig. 6(b)).

The strong variations of $Nu_{i,u}$ shown in Figs. 9 and 10 contrast sharply with the periodic traveling waves that occur at lower Gr (and lower Re) [16]. Previously [16], the amplitudes of the multiple maxima and minima values of the heat transfer on both surfaces

were essentially of constant magnitude and occurred at the same location (i.e. at one value of x , there is a maximum on one surface and a minimum on the other surface). For larger Gr (and larger Re) there is now no longer a direct relationship between the maxima and minima (Fig. 10(a)), and the heat transfer is due to the complex interaction of the full three dimensional flow structures. The spatially averaged Nusselt numbers (over the lower and upper surfaces) vary slightly with time in an irregular manner (not shown) and have approximate values of $\bar{Nu}_l = 4.8$ and $\bar{Nu}_u = 2.6$, with much of the difference between the values resulting from the thermally developing flow on the lower surface. As noted above, this is in contrast to the result for smaller values of both Re and Gr which have variations with time that are regular [16]. In terms of comparisons between the present study and ref. [16], we note that the different thermal boundary conditions at the inlet, as specified in the introduction, are responsible for some of the differences.

The average Nusselt number on the upper surface \bar{Nu}_u (for $Re = 100$) is significantly larger than the steady value of 1.7 for $Re = 250$. The increased heat transfer for $Re = 100$ is due to the earlier onset of the instability and the subsequent downstream development of the complex three dimensional, unsteady flow. On the lower surface, although there is unsteadiness for $Re = 100$, the value of approximately 4.8 for \bar{Nu}_l is close to the steady value of 5.1 at $Re = 250$.

Other cases. Calculations were also carried out at lower Reynolds numbers (still at $Gr = 1.25 \times 10^5$ and $\varepsilon = 0.01$). For $Re = 75$, the flow pattern is even more complex but it still consists of the longitudinal and transverse roll structures discussed above. Indeed, in the thermally developing region near the inlet the

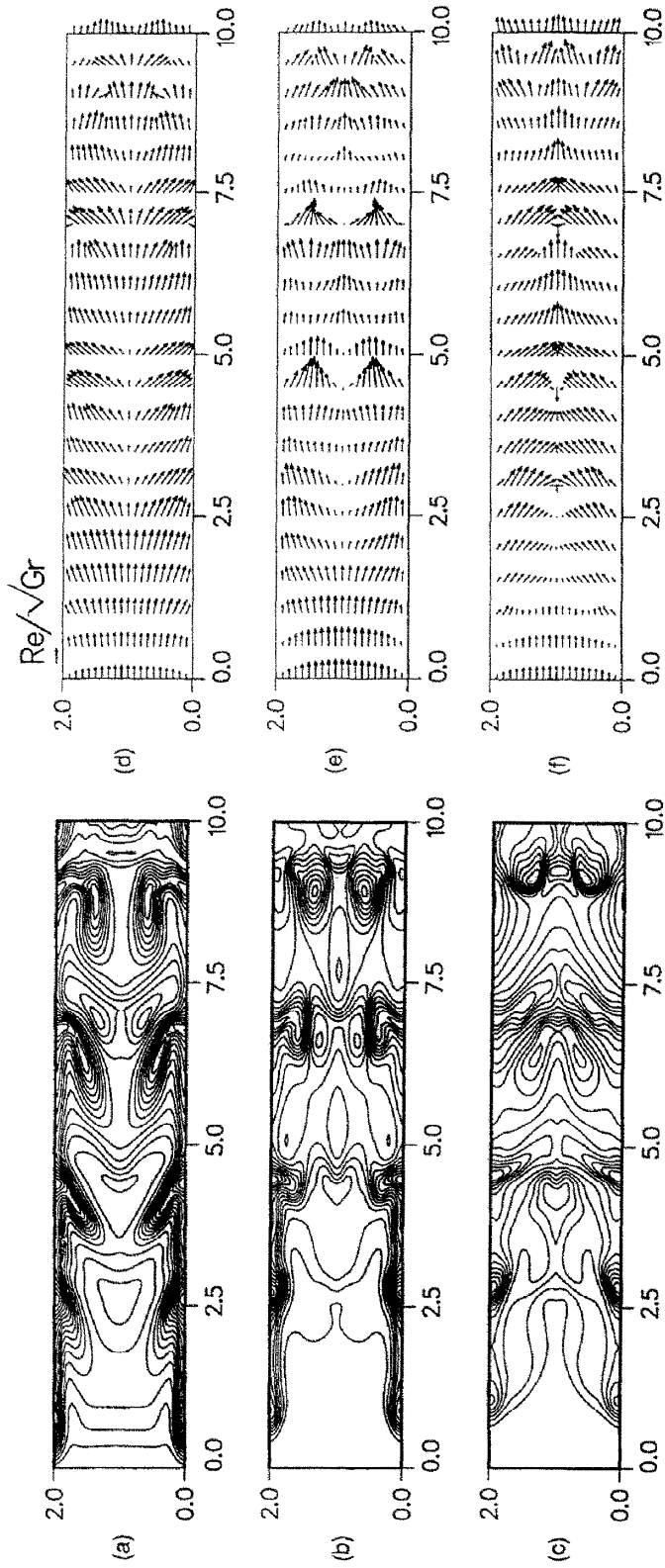


FIG. 8. Temperature and velocity fields on horizontal (xz) planes for $Re = 100$, $Gr = 1.25 \times 10^5$, $\epsilon = 0.01$, $\tau = 80$: (a)–(c) temperature contours (min 0.05, max 0.95, inc 0.05) at $y = 0.22$, 0.5, and 0.78, respectively; (d)–(f) velocity arrows (reference arrow length corresponds to average dimensionless velocity at channel inlet: Re/\sqrt{Gr}) at $y = 0.22$, 0.5, and 0.78, respectively.

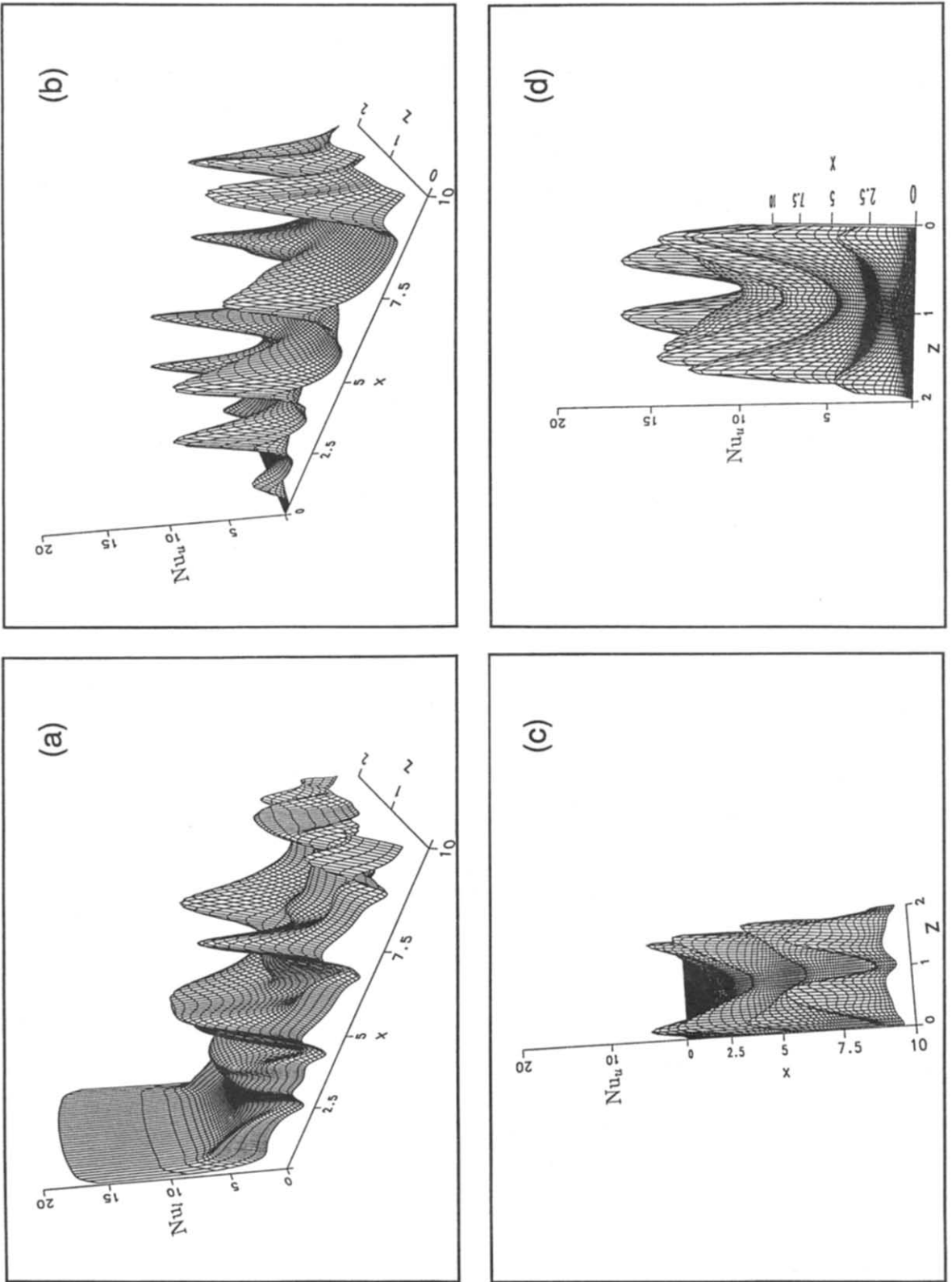


Fig. 9. Surface maps of the local Nusselt numbers for $Re = 100$, $Gr = 1.25 \times 10^5$, $\epsilon = 0.01$; (a) on the lower hot surface; (b)–(d) on the upper cold surface.

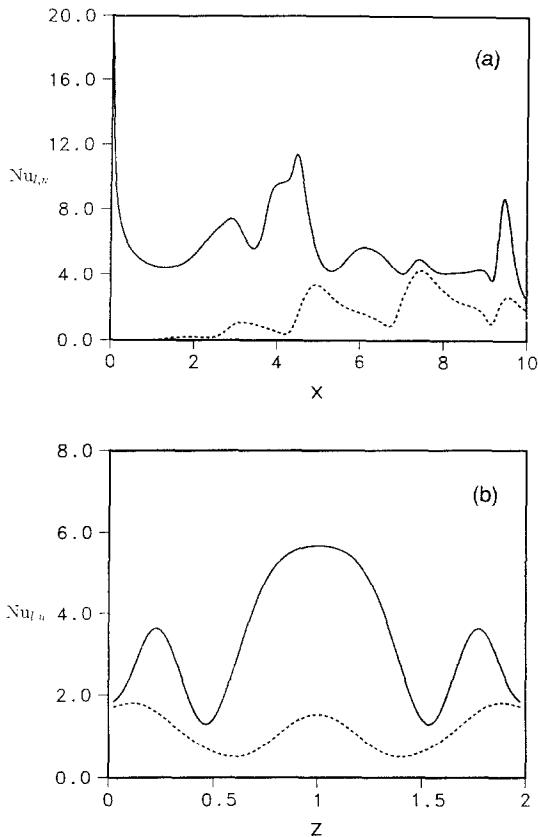


FIG. 10. Local Nusselt numbers on the lower hot surface (—) and the upper cold surface (---) of the channel for $Re = 100$, $Gr = 1.25 \times 10^5$, $\varepsilon = 0.01$, $t = 80$; (a) for the vertical central plane ($z = 1.0$); (b) for a transverse cross-sectional ($y-z$) plane ($x = 6.18$).

instability is more pronounced and the transverse wave structure downstream is more vigorous (not shown). Calculations at lower values of Re for the same Gr resulted in a loss of symmetry about $z = 1.0$ which could not be resolved with grid and time step refinement. Results were also obtained for $Re = 75$ and a smaller Grashof number, $Gr = 5.0 \times 10^4$. For this lower Grashof number the instability begins further downstream and the flow pattern is not as complex (not shown).

Other calculations were performed for $Gr = 5.0 \times 10^4$, $Re = 100$, and $\varepsilon = 0.01$. For this condition there is no instability in the upstream portion of the channel; the transverse wave structure is intermediate between the results shown in Figs. 3(a) and 7(a) which are for $Re = 250$ and 100, respectively, with $Gr = 1.25 \times 10^5$.

Grid sensitivity. The spatial grid size and time step sensitivities of the results were evaluated. The results shown for $Re = 250$, $Gr = 1.25 \times 10^5$ used $101 \times 21 \times 41$ grids (Δx , Δy , Δz) = (0.101, 0.0526, 0.0513) and a time step of 0.02. Grid sensitivity tests showed results for \bar{Nu}_l that differed by less than 1% from results obtained on grids of $101 \times 31 \times 41$, $101 \times 41 \times 41$, $101 \times 21 \times 51$, and $121 \times 31 \times 41$; \bar{Nu}_u

deviated by less than 3%. Local Nusselt numbers showed a similar small grid dependence except for the peak values that are near the side walls on the upper surface at $x = 6.01$ (shown in Fig. 4(b)). These peak values had differences of 28, 41, 14 and 32% for the above cited grids when compared with the peak values for the $101 \times 21 \times 41$ grid. For Nu_u differences of 4, 4, 7, and 5% resulted at the minimum values for the above four grids.

The results shown for $Re = 100$, $Gr = 1.25 \times 10^5$ used $171 \times 31 \times 41$ (x, y, z) spatial grids and a time step of 0.02. Comparisons of the local Nusselt numbers on the transverse plane at $x = 6.0$ and $t = 78$, using a $201 \times 31 \times 41$ spatial grid and the same time step showed excellent agreement (better than 1.0%) over the lower surface; maximum differences of 4 and 8% were obtained over the upper surface at the center, $z = 1.0$, and near the side walls, $z = 0.0$ and $z = 2.0$, respectively. The differences are restricted to the isolated locations noted. For comparisons of the axial variation of the local Nusselt number on the central longitudinal plane, $z = 1.0$, there is excellent agreement for $x < 6$, but significant disagreement results for $x > 9$, i.e. near the exit where the unknown exit boundary condition affects the flow (Bottaro [19]). Calculations were also carried out using a $171 \times 41 \times 51$ grid and a time step of 0.02. Comparisons with the $171 \times 31 \times 41$ grid for Nu_l on the transverse plane at $x = 6.0$ and $t = 74$ show very good agreement with a maximum difference of 2% occurring at the three peaks (Fig. 10(b)). Comparisons of Nu_u show good agreement with a maximum difference of 10% which occurs at the central peak. The axial variation of $Nu_{l,u}$ for the two axial grid spacings discussed above ($171 \times 31 \times 41$ and $201 \times 31 \times 41$) resulted in differences similar to the 1.0% difference noted above. The axial variation of $Nu_{l,u}$ for the two transverse grid spacings (41×51 and 31×41) again showed good agreement for $x < 6$; maximum differences of approximately 10% appear near $x = 7$.

The computing time required to advance a single time step varied during the course of the simulation depending on the state of the phenomena. During the period of initial growth of the instability, a large number of iterations were required; e.g. 30. Once the instability was established, the number was reduced to approximately 10. These values depend on the convergence criteria which are specified in ref. [16]. For a $171 \times 41 \times 51$ grid the cpu time per iteration on a Cray Y-MP was 35 s. The time step sensitivity of the results was checked by making calculations with various time steps; in particular, excellent agreement between the results for $\Delta t = 0.02$ and $\Delta t = 0.03$ was obtained.

Large temperature differences ($\varepsilon = 2.33$)

In the variable property results for helium the parameters Re , Gr , and Pr were evaluated at the inlet gas temperature which was constant for both the high

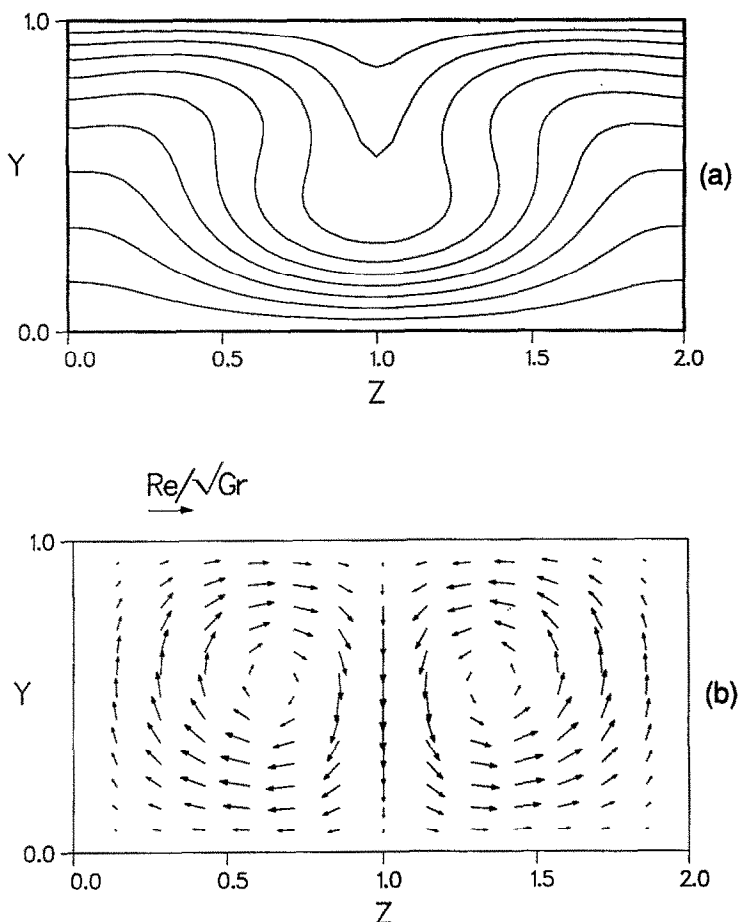


FIG. 11. Temperature and velocity fields in a transverse cross-sectional (yz) plane ($x = 6$) for $Re = 100$, $Gr = 1.25 \times 10^5$, $\varepsilon = 2.33$; (a) temperature contours (min 0.1, max 0.9, inc 0.1); (b) velocity arrows (reference arrow length corresponds to average dimensionless velocity at channel inlet: Re/\sqrt{Gr}).

and low temperature cases. The conditions, $\varepsilon = 2.33$ (lower surface temperature of 1000 K), $Re = 100$, and $Gr = 1.25 \times 10^5$, result in steady flow with a longitudinal roll instability (Figs. 11(a) and (b); $x = 6$). The instability begins at $x \approx 3.0$ (Fig. 12(a)) which is approximately equal to the x position for the initiation of the instability for the constant property case ($\varepsilon = 0.01$, Fig. 7(a)). However, for the high temperature case (Fig. 12(a)) the development of the instability downstream of the initiation point is not as pronounced as it is for the low temperature case (Fig. 7(a)). Note that now there is little axial variation of the temperature and velocity fields beyond the onset of the instability (Figs. 12(a) and (b)), and the complex variations in $Nu_{1,a}$ along the central vertical plane for constant properties (Fig. 10(a)) are no longer present for variable properties (Fig. 13(a)). This is a consequence of the larger values of the thermal conductivity and viscosity for high temperatures. The single maximum in Nu_1 and the corresponding minimum in Nu_a in the transverse cross-section (yz plane, $x = 6$) of Fig. 13(b) are related to the two longitudinal rolls shown in Fig. 11(b). This contrasts with the

triple peak in Nu_1 (Fig. 10(b)) previously noted for the constant property case.

CONCLUSIONS

This work is a study of the three dimensional flow patterns and the heat transfer in a horizontal channel with applications to chemical vapor deposition. For some reactor operating conditions, thermal instabilities occur resulting in large gradients in all three directions which can be time dependent. The results include longitudinal roll structures in a steady flow as well as traveling transverse waves and longitudinal rolls that are present in an unsteady flow. For small temperature differences ($\varepsilon = 0.01$), moderate Reynolds numbers (≤ 100), and large Grashof numbers (125000), the flow patterns are complex and time dependent. For larger Reynolds numbers (≈ 250), the flow pattern is simpler, consisting of steady longitudinal rolls. For very large Reynolds numbers, the thermal instability is convected far downstream and may not be present in the channel. For the large tem-

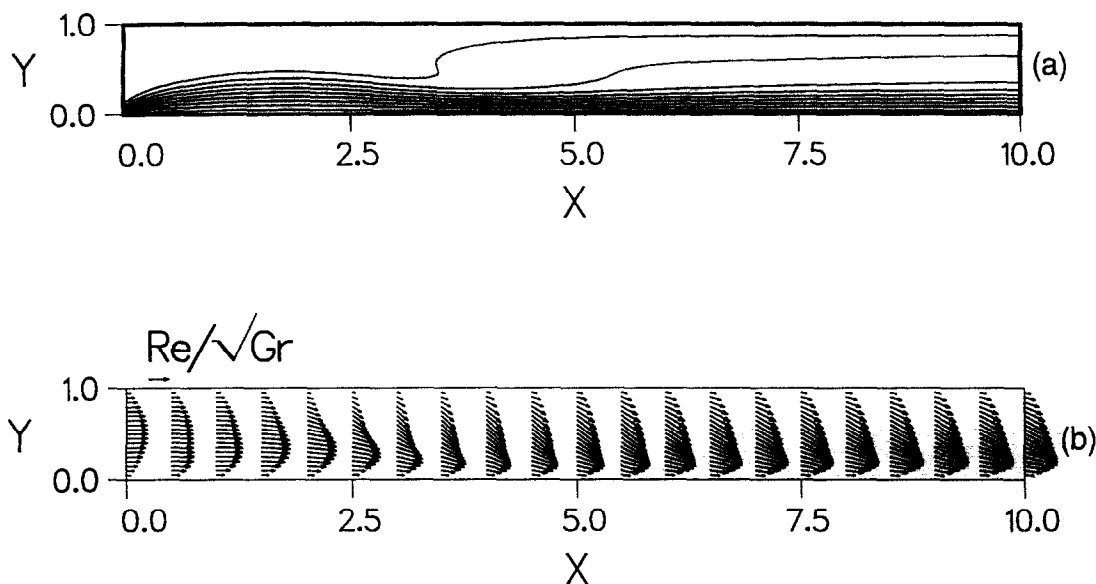


FIG. 12. Temperature and velocity fields in the vertical central (xy) plane ($z = 1.0$) of the channel for $Re = 100$, $Gr = 1.25 \times 10^5$, $\varepsilon = 2.33$; (a) temperature contours (min 0.1, max 0.9, inc 0.1); (b) velocity arrows (reference arrow length corresponds to average dimensionless velocity at channel inlet: Re/\sqrt{Gr}).

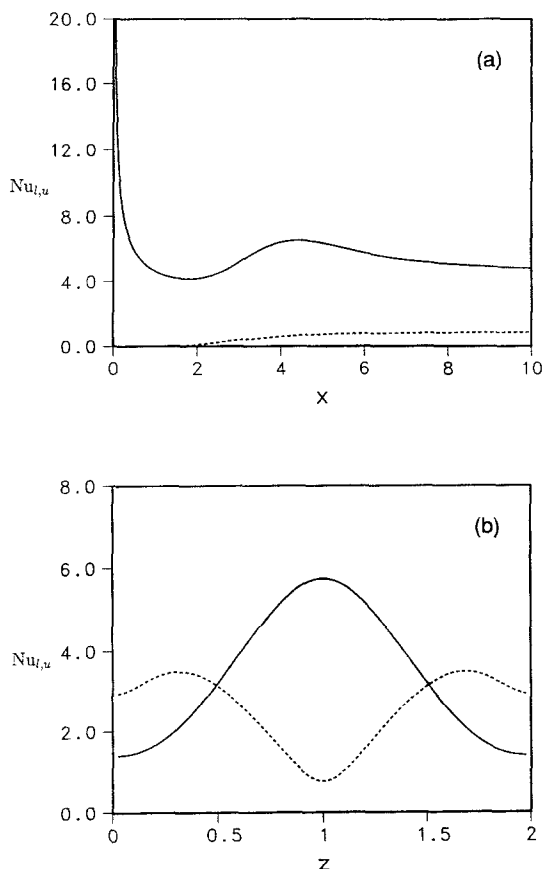


FIG. 13. Local Nusselt numbers on the lower hot surface (—) and the upper cold surface (---) of the channel for $Re = 100$, $Gr = 1.25 \times 10^5$, $\varepsilon = 2.33$; (a) for the vertical central plane ($z = 1.0$); (b) for a transverse cross-sectional (yz) plane ($x = 6$).

perature difference case ($\varepsilon = 2.33$, $Re = 100$, and $Gr = 125000$), the effects of variable fluid properties (helium) result in a less complex steady flow consisting of longitudinal rolls. The results demonstrate the occurrence of phenomena that can lead to considerable variations in deposition rates and profiles in chemical vapor deposition channel reactors.

REFERENCES

1. K. F. Jensen, Modeling of chemical vapor deposition reactors, *Proc. 9th Int. Conf. on Chemical Vapor Deposition*, pp. 3–20 (1984).
2. M. E. Coltrin, R. J. Kee and J. A. Miller, A mathematical model of the coupled fluid mechanics and chemical kinetics in a chemical vapor deposition reactor, *J. Electrochem. Soc.* **131**(2), 425–434 (1984).
3. L. J. Giling, Gas flow patterns in horizontal epitaxial reactor cells observed by interference holography, *J. Electrochem. Soc.* **129**(3), 634–644 (1982).
4. H. Moffat and K. F. Jensen, Three-dimensional flow effects in silicon CVD in horizontal reactors, *J. Electrochem. Soc.* **135**(2), 459–471 (1988).
5. D. L. Fotiadis, M. Bockholt, K. F. Jensen and W. Richter, Flow and heat transfer in CVD reactors: comparison of Raman temperature measurements and finite element model predictions, *J. Crystal Growth* **100**, 577–599 (1990).
6. C. R. Kleijn, Th. H. van der Meer and C. J. Hoogendoorn, A mathematical model for LPCVD in a single wafer reactor, *J. Electrochem. Soc.* **136**(11), 3423–3432 (1989).
7. K. C. Chiu and F. Rosenberger, Mixed convection between horizontal plates—I. Entrance effects, *Int. J. Heat Mass Transfer* **30**, 1645–1654 (1987).
8. J. Ouazzani and F. Rosenberger, Three-dimensional modeling of horizontal chemical vapor deposition I. MOCVD at atmospheric pressure, *J. Crystal Growth* **100**, 545–576 (1990).
9. J. Van de Ven, G. M. J. Rutten, M. J. Raaijmakers and

- L. J. Giling, Gas phase depletion and flow dynamics in horizontal MOCVD reactors, *J. Crystal Growth* **76**, 352–372 (1986).
10. T. A. Nyce, J. Ouazzani, A. Durand-Daubin and F. Rosenberger, Mixed convection in a horizontal rectangular channel—experimental and numerical velocity distributions, *Int. J. Heat Mass Transfer* **35**, 1481–1494 (1992).
 11. K. F. Jensen, E. O. Einset and D. I. Fotiadis, Flow phenomena in chemical vapor deposition of thin films, *Ann. Rev. Fluid Mech.* **23**, 197–232 (1991).
 12. C. R. Kleijn, Transport phenomena in chemical vapor deposition reactors, Ph.D. Thesis, Delft University of Technology (1991).
 13. K. S. Gage and W. H. Reid, The stability of thermally stratified plane Poiseuille flow, *J. Fluid Mech.* **33**(1), 21–32 (1968).
 14. R. M. Clever and F. H. Busse, Instabilities of longitudinal rolls in the presence of Poiseuille flow, *J. Fluid Mech.* **229**, 517–529 (1991).
 15. J. K. Platten and J. C. Legros, *Convection in Liquids*, chap. 8. Springer, Berlin (1984).
 16. G. Evans and R. Greif, Unsteady three-dimensional mixed convection in a heated horizontal channel flow with applications to chemical vapor deposition, *Int. J. Heat Mass Transfer* **34**, 2039–2051 (1991).
 17. A. D. Gosman and W. M. Pun, Calculation of Recirculating Flow, Lecture Notes, Imperial College of Science and Technology, London, England (1973).
 18. S. V. Patankar, *Numerical Heat Transfer and Fluid Flow*. McGraw-Hill, New York (1980).
 19. A. Bottaro, A note on open boundary conditions for elliptic flows, *Numerical Heat Transfer, Part B* **18**, 243–256 (1990).